Effective Markovian description of decoherence in bound systems

A. S. Sanz
Instituto de Física Fundamental (IFF–CSIC), Serrano 123, 28006 - Madrid, Spain

(Dated: February 18, 2014)

Effective descriptions accounting for the evolution of quantum systems that are acted on by a bath are desirable. As the number of bath degrees of freedom increases and full quantum simulations turn out computationally prohibitive, simpler models become essential to understand and gain an insight into the main physical mechanisms involved in the system dynamics. In this regard, vibrational decoherence of an I_2 diatomics is tackled here within the framework of Markovian quantum state diffusion. The I_2 dynamics are analyzed in terms of an effective decoherence rate, Λ, and the specific choice of the initial state, in particular, Gaussian wave packets and two-state superpositions. It is found that, for Markovian baths, the relevant quantity regarding decoherence is the product of friction (η) and temperature (T); there is no distinction between varying one or the other. It is also observed that decoherence becomes faster as the energy levels involved in the system state correspond to higher eigenvalues. This effect is due to a population redistribution during the dynamical process and an eventual irreversible loss of the initial coherence. These results have been compared with those available in the literature from more detailed semiclassical IVR simulations, finding a good agreement.

Keywords: Markovian dynamics; quantum state diffusion; vibrational decoherence; dephasing; stochastic quantum trajectory

I. INTRODUCTION

Consider a quantum system (S) coupled to a quantum bath (B). As it is commonly done in open quantum system theory,[1] let us also assume that initially the system and bath are uncorrelated. The wave function of the total system, S+B, can then be expressed in terms of a general, factorizable product state:

$$|\Psi\rangle = |\Psi_{\rm S}\rangle \otimes |\Psi_{\rm B}\rangle. \tag{1}$$

As time proceeds, the interaction between system and bath makes this state to become nonseparable or entangled. This process can be understood as an effective transfer or flow of coherence between both subsystems, which results in a gradual quenching of any interference feature associated with the quantum system S. This phenomenon is what we usually call decoherence. Typically, it takes place at time scales shorter than energy relaxation, i.e., before the system energy starts flowing (dissipating) towards the bath. Depending on the nature of the bath and the system–bath coupling strength, the system coherence loss may go from partial (or even total) reversibility (recurrences) to total irreversibility (Markovianity). The latter is usually related to the emergence of the classical world,[2,3] because the "classical" law of addition of probabilities is recovered.

Real systems are not fully isolated in nature. Therefore, given the major role played by quantum coherence at microscopic and mesoscopic scales in different areas of physics, chemistry, and biology, an appropriate characterization of the system–bath interaction is very important. Very detailed and accurate simulations of the corresponding systems are thus essential to study, analyze, and understand the related phenomena and effects. This has motivated the development of highly sophisticated numerical techniques, including classical and semiclassical treatments whenever the amount of degrees of freedom involved make computationally prohibitive full quantum-mechanical treatments. This, however, does not necessarily mean that we fully understand the system dynamics. The complexity of these models often makes them intractable from an analytical viewpoint, hiding the main mechanisms that come into play. Hence alternative (but complementary) simpler models based on master equations that capture the essence of the system behavior are desirable; they provide us with the insight necessary to better understand such underlying mechanisms.

To illustrate that assertion, consider the Caldeira–Leggett model used in Wang et al.[4] to describe the quenching of vibrational interference effects of an I_2 diatomics coupled to a bath of harmonic oscillators. This bath is characterized by a spectral density with ohmic form. The characteristic frequency chosen for this bath is $\omega_c = 20$ cm^{-1}, while the largest frequency of the bath modes is $\omega_m = 100$ cm^{-1} (a total of 20 to 40 of these modes were considered in their simulations). As mentioned above, full quantum simulations are computationally prohibitive in these cases, so a way to tackle the issue is by means of the semiclassical initial value representation (SC-IVR) method.[5,6] Apart from its well-known computational advantages, this technique is also very convenient and interesting regarding the quantum-to-classical transition: it provides us with a systematic procedure to add quantum coherence to classical molecular dynamics simulations and therefore to distinguish between classical and quantum coherence.[7,8] The analysis reported in Wang et al.[4] precisely pursues this simple idea (for a similar application to the two-slit experiment, see Gelabert et al.[9]) As the bath temperature and/or system–bath coupling strength are increased, the system gradually loses its coherence, exhibiting a "classical-like" behavior. Physically, this manifests as a quenching of

interference features; computationally, one finds a better agreement between the SC-IVR and bare classical molecular dynamics simulations (linearized IVR).

Based on such results, here we address the following question: can the behaviors reported in Wang et al.[4] be properly described in terms of a simple master equation? Among the different approaches available in the literature to address this problem,[1] we have considered the quantum state diffusion approach[10–16] due to three reasons: (*i*) it preserves the appealing concept of quantum state or wave function as the main descriptor of the system and its time evolution, (*ii*) it stresses the "flavor" of the concept of dephasing, i.e., decoherence not only comes from the interaction with a bath but also from the incoherence among a large (statistical) number of realizations, and (*iii*) from a technical (numerical) viewpoint, it is relatively simple to implement (simpler than dealing with density matrices in configuration space), and yet it still captures the physics of the phenomenon, namely decoherence.

With respect to *ii*, notice that within this theoretical framework, the expectation value of an operator $\hat{\mathcal{O}}$ that describes an observable O arises from an average:

$$\langle\hat{\mathcal{O}}\rangle(t) = \frac{1}{N}\sum_{i=1}^{N}\langle\Psi_i(t)|\hat{\mathcal{O}}|\Psi_i(t)\rangle, \tag{2}$$

with the subscript i labeling each particular realization of the state vector, $|\Psi_i\rangle$, and where N is the total number of realizations considered; each single realization $\langle\hat{\mathcal{O}}\rangle_i(t) \equiv \langle\Psi_i(t)|\hat{\mathcal{O}}|\Psi_i(t)\rangle$ describes the time evolution of the expectation value of $\mathcal{O}$ associated with the system state vector $|\Psi_i\rangle$. Each one of these single realizations constitutes a *stochastic quantum trajectory* analogous to those proposed by Carmichael for optical systems,[17] although $|\Psi_i\rangle$ displays a stochastic dynamics throughout its full evolution. These trajectories describe different physical quantities depending on which operator $\hat{\mathcal{O}}$ is chosen, being unique for each $|\Psi_i\rangle$ vector. This makes an important difference with respect to other types of quantum trajectories, such as Bohmian trajectories,[18,19] which are not related to a particular operator, but to a single state vector in configuration representation.

This work has been organized as follows. The main theoretical aspects of the quantum state diffusion approach as well as its adaptation to the problem dealt with here are briefly summarized in Section II. The system and numerical details involved in the simulations considered here are presented in Section III. In Section IV the main results are discussed. Finally, in Section V, the main conclusions arising from this work are summarized.

II. THEORY

A. General aspects

Consider the dissipative dynamics of a system described within the framework of the Lindblad approach.[1] Compared with other approaches available in the literature, Lindblad's one gathers two interesting properties:

(i) it does not arise from any particular representation, thus being the most abstract approach that we can find (Redfield's approach, for example, comes from the energy representation, although later on one can recast it in other representations) and

(ii) it provides us with the most general form of equation of motion for the density matrix, which satisfies complete positivity.

In this approach, the evolution of the system (reduced) density matrix $\hat{\rho}_{\rm S}$ is described by the usual Liouvillian term plus a dissipator, which accounts for the bath effective action over the system. More specifically, Lindblad's equation reads as

$$\frac{d\hat{\rho}_{\rm S}(t)}{dt} = -\frac{i}{\hbar}[\hat{H}, \hat{\rho}_{\rm S}(t)] + \mathcal{D}[\hat{\rho}_{\rm S}(t)], \tag{3}$$

where $\hat{H}$ is the Hamiltonian associated with the bare (free) system and

$$\mathcal{D}(\hat{\rho}_{\rm S}) \equiv \sum_j \Lambda_j \left(2\hat{L}_j\hat{\rho}_{\rm S}\hat{L}_j^\dagger - \hat{L}_j^\dagger\hat{L}_j\hat{\rho}_{\rm S} - \hat{\rho}_{\rm S}\hat{L}_j^\dagger\hat{L}_j\right) \tag{4}$$

is the dissipator. In this latter expression, the $\hat{L}_j$ represent the so-called Lindblad operators, which describe how the bath specifically acts over the system. The relevance of this action is given by the corresponding system–bath coupling strength constants Λ_j: the larger the value of Λ_j, the faster the decoherence/dissipation induced by $\hat{L}_j$ occurs.

The Lindblad eq. 3 can be recast in the form of a state vector equation[10–16] in the Itô form[20,21]

$$|d\Psi\rangle = |v\rangle dt + \sum_j |u_j\rangle d\xi_j. \tag{5}$$

In this diffusion-like equation, $|v\rangle$ is a deterministic drift term, while the $d\xi_j$ elements denote independent complex Wiener processes associated with the action of stochastic bath fluctuations over the system, such that $\langle\Psi|u_j\rangle = 0$, for all j, to ensure the state vector normalization. The means of these Wiener processes over both the distribution and the fluctuations are assumed to satisfy

$$E(d\xi_j) = 0, \tag{6a}$$
$$E(d\xi_j d\xi_k) = 0, \tag{6b}$$
$$E(d\xi_j^* d\xi_k) = 2\delta_{jk}dt, \tag{6c}$$

i.e., these Wiener processes have zero mean and variance $\sqrt{dt}$.

Physically, eq. 5 describes a single, stochastic realization (or time propagation) of the quantum system state vector. Any expectation value obtained from this realization is called a *stochastic quantum trajectory* because one

can keep track of the corresponding property in time, in analogy to classical trajectories.[22] In order to obtain an appropriate description of the system dissipative dynamics, it is necessary to carry out a large number of such realizations; information about the influence of the bath over the system (decoherence or dissipation) is extracted from the average over the corresponding quantum trajectories. Hence, the bath effects over the system can be somewhat understood in terms of the dephasing displayed by the different realizations of the vector state, which leads to its loss of coherence and eventually also to its relaxation (dissipation). This picture summarizes the role of the reduced density matrix as a statistical descriptor of the system dynamics, since it can be recast as

$$\hat{\rho}_{\rm S} = E(|\Psi\rangle\langle\Psi|) = \frac{1}{N}\sum_{i=1}^{N}|\Psi_i\rangle\langle\Psi_i|. \tag{7}$$

Taking into account these facts, particularly eq. 7, after some algebra one obtains (see, for example, Gisin and Percival[13] for a simple derivation) an explicit functional form for the drift and stochastic terms of eq. 5:

$$\begin{aligned} |v\rangle &= -\frac{i}{\hbar}\hat{H}|\Psi\rangle \\ &\quad + \sum_j \Lambda_j\Big(2\langle\hat{L}_j^\dagger\rangle_\Psi\hat{L}_j - \hat{L}_j^\dagger\hat{L}_j - \langle\hat{L}_j^\dagger\rangle_\Psi\langle\hat{L}_j\rangle_\Psi\Big)|\Psi\rangle, \end{aligned} \tag{8}$$

$$|u_j\rangle = \sqrt{\Lambda_j}\left(\hat{L}_j - \langle\hat{L}_j\rangle_\Psi\right)|\Psi\rangle, \tag{9}$$

respectively, with $\langle\hat{L}_k\rangle_\Psi \equiv \langle\Psi|\hat{L}_j|\Psi\rangle$ being the expectation value of the Lindblad operator $\hat{L}_j$ with respect to the state vector $|\Psi\rangle$ at time t. Substituting these terms into eq. 5 gives rise to the Itô equation:

$$\begin{aligned} |d\Psi\rangle &= -\frac{i}{\hbar}\hat{H}|\Psi\rangle dt \\ &\quad + \sum_j \Lambda_j\Big(2\langle\hat{L}_j^\dagger\rangle_\Psi\hat{L}_j - \hat{L}_j^\dagger\hat{L}_j - \langle\hat{L}_j^\dagger\rangle_\Psi\langle\hat{L}_j\rangle_\Psi\Big)|\Psi\rangle dt \\ &\quad + \sum_j \sqrt{\Lambda_j}\left(\hat{L}_j - \langle\hat{L}_j\rangle_\Psi\right)|\Psi\rangle d\xi_j. \end{aligned} \tag{10}$$

B. Reduced Caldeira–Leggett model

In order to make practical use of eq. 10, we still need to define the functional form displayed by the Lindblad operators. Let us therefore go back to the Caldeira–Leggett model. Within this model, system and bath are assumed to be coupled bilinearly, i.e., by means of terms of the form xX_i, where x and X_i denote the system and ith bath coordinates, respectively. In the high–temperature regime, this model can be recast in terms of a master equation:[1,23]

$$\frac{d\hat{\rho}_{\rm S}}{dt} = -\frac{i}{\hbar}[\hat{H},\hat{\rho}_{\rm S}] - \frac{i\eta}{\hbar}[\hat{x},\{\hat{p},\hat{\rho}_{\rm S}\}] - \frac{2m\eta k_B T}{\hbar^2}[\hat{x},[\hat{x},\hat{\rho}_{\rm S}]] \tag{11}$$

where the first term represents the system unitary evolution, the second its relaxation, and the third its decoherence. Although this equation is Markovian, it is not of the Lindblad form. Nonetheless, at high temperatures, one can add to (11) the term

$$-\frac{\eta}{8mk_BT}[\hat{p},[\hat{p},\hat{\rho}_{\rm S}]], \tag{12}$$

which is relatively small. The Lindblad form appears after diagonalizing the corresponding dissipator, which renders the associated Lindblad operators.[1]

A simpler way to proceed than diagonalizing, however, consists of assuming that at relatively classical regimes, i.e., when Planck's constant is relatively small compared with the actions involved and the object is massive, the third term on the right-hand side of eq. 11 is much larger than the second one. This allows us to simplify eq. 11[24,25] as

$$\begin{aligned} \frac{d\hat{\rho}_{\rm S}}{dt} &= -\frac{i}{\hbar}[\hat{H},\hat{\rho}_{\rm S}] - \frac{2m\eta k_BT}{\hbar^2}[\hat{x},[\hat{x},\hat{\rho}_{\rm S}]] \\ &= -\frac{i}{\hbar}[\hat{H},\hat{\rho}_{\rm S}] + \frac{2m\eta k_BT}{\hbar^2}\Big(2\hat{x}\hat{\rho}_{\rm S}\hat{x} - \hat{x}^2\hat{\rho}_{\rm S} - \hat{\rho}_{\rm S}\hat{x}^2\Big). \end{aligned} \tag{13}$$

This equation, already in the Lindblad form, is known as the reduced Caldeira–Leggett model.[1] Its range of validity can be easily inferred as follows. The hypothesis considered to obtain (13) is equivalent to the previous assumption that (12) is small compared with the third term of (11). On the other hand, if ω is some characteristic frequency associated with the system, one would expect that the corresponding momenta go like $p \sim m\omega x$, approximately. Substituting this estimate of the momentum into eq. 12 and then making use of the above assumptions, we find

$$\frac{4k_BT}{\hbar\omega} \gg 1. \tag{14}$$

Accordingly, eq. 13 is valid whenever temperatures satisfy this relation.

Following the state vector approach introduced in Section II A, eq. 13 can be recast as a quantum stochastic differential equation, namely:

$$\begin{aligned} |d\Psi\rangle &= -\frac{i}{\hbar}\hat{H}|\Psi\rangle dt - \Lambda\left(x - \langle x\rangle\right)^2|\Psi\rangle dt \\ &\quad + \sqrt{\Lambda}\left(x - \langle x\rangle\right)|\Psi\rangle d\xi, \end{aligned} \tag{15}$$

with one Lindblad operator, $\hat{L} = \sqrt{\Lambda}\,\hat{x}$, and where the system–bath coupling strength is given by the decoherence rate:

$$\Lambda = \frac{2m\eta k_BT}{\hbar^2}, \tag{16}$$

with units of $(\text{space})^{-2}\times(\text{time})^{-1}$. This rate provides us with an estimate of the time scales at which the correlation (coherence) between two points in configuration

space is lost. For example, for two points separated a distance ℓ, this time scale will be of the order of $1/\Lambda\ell^2$.

The numerical simulations reported in Section IV constitute a test of the feasibility and applicability of eq. 13 to study in a simplified fashion systems afforded by the full Caldeira–Leggett model. Notice that in the ranges of temperature where this description is valid, one has an interesting, effective tool to probe open quantum system dynamics, where all bath effects (temperature and friction) are enclosed within a single parameter, namely the decoherence rate Λ. Because the bath dynamics are not explicitly considered, there is a remarkable reduction of the computational time demand with respect to full system–bath treatments (classical or semiclassical). In this sense, it is worth stressing that the state vector approach could be advantageously used to explore the system dynamics in some ranges of parameters of interest, previous to full, more detailed dynamical simulations. On the contrary, as a feedback, the latter type of calculations could be used to design and implement better Lindblad operators that would help to improve the model based on eq. 13 and eventual interpretations relying on it.

III. NUMERICAL DETAILS

As in Wang et al.[4], here we have analyzed the gradual coherence loss displayed by the radial distribution function of the I_2. The lowest electronic energy surface describing this system can be modeled by a Morse function along the radial direction (here denoted by x):

$$V(x) = D\left[1 - e^{-\alpha(x-x_e)}\right]^2, \tag{17}$$

with parameters $D = 1.2547 \times 10^4$ cm^{-1}, $\alpha = 1.8576$ Å^{-1}, and $x_e = 2.6663$ Å. This Morse oscillator supports about 120 bound states and has a harmonic frequency

$$\omega_0 = \sqrt{\frac{2\alpha^2 D}{m}} \approx 214.6 \text{ cm}^{-1} = 40.451 \text{ ps}^{-1}, \tag{18}$$

where m is the I_2 reduced mass ($m = m_0/4$, with $m_0 = 4.22\times10^{-22}$ g being the I_2 mass). To compare with Wang et al.[4], first we have considered the dynamics displayed by a Gaussian wave packet:

$$\Psi_0(x) = \left(\frac{1}{2\pi\sigma^2}\right)^{1/4} e^{-(x-x_0)^2/4\sigma_0^2 + ip_0(x-x_0)/\hbar}, \tag{19}$$

with parameters $x_0 = 2.4$ Å, $p_0 = 0$, and $\sigma_0^2 = \hbar/2m\omega_0$, under the action of the Morse potential (eq. 17) and a stochastic noise satisfying the properties of eq. 6. Several two-state superpositions have also been studied in order to understand the relationship between coherence and population dynamics.

The scheme followed to solve numerically eq. 15 consists of attacking separately the Hamiltonian and the diffusive parts and then combining them together,[26–28] thus following a strategy somewhat analogous to operate in the interaction picture. The Hamiltonian part (first term on the right-hand side of eq. 15) is integrated by making use of the split-operator scheme[29–31] combined with the fast Fourier method.[32] The diffusive part [second and third terms on the right-hand side of eq. 15] is separately integrated with a second-order Runge-Kutta algorithm adapted to stochastic processes.[33] The updated wave function results from the addition of both solutions. A single realization of the state vector $|\Psi\rangle$ is obtained by proceeding recursively in this manner until concluding the time propagation. In the calculations, a total of 2500 realizations for the Gaussian wave packet and 2000 for the superpositions have been considered. These numbers have been found to be optimal for the quantities computed and presented here, although even more realizations could be necessary in other cases. This happens, for example, in the calculation of energy-level populations and coherences for the Gaussian wave packet (19). The energy levels involved in this Gaussian state are higher than those intervening in the two-state superpositions considered below, so obtaining smoothly converged quantum trajectories for them requires a higher number of realizations than for the latter.

IV. RESULTS AND DISCUSSION

A. Wave packet dynamics

In order to test the accuracy and stability of the numerical algorithm, first a trial simulation has been run with the initial wave packet (19) and $\Lambda = 10^{-8}$ (given for simplicity in atomic units: 1 a.u. (Λ) = 147.6 Å^{-2}fs^{-1} $\approx 1.5 \times 10^{32}$ cm^{-2}s^{-1}). This Λ value is relatively small to have important effects on the unitary part of the algorithm and therefore allows us to obtain a close solution to a noise-free ($\Lambda = 0$) propagation. A series of snapshots of the averaged probability density

$$\begin{aligned}\rho_S(x,t) &= \langle x|\hat{\rho}_S(t)|x\rangle \\ &= \langle x|\left[\frac{1}{N}\sum_{i=1}^{N}|\Psi_i(t)\rangle\langle\Psi_i(t)|\right]|x\rangle \\ &= \frac{1}{N}\sum_{i=1}^{N}\langle x|\Psi_i(t)\rangle\langle\Psi_i(t)|x\rangle,\end{aligned} \tag{20}$$

with $N = 2500$, spanning a time of 160 fs is displayed in Fig. 1. This time covers the first harmonic vibrational period ($\tau_0 = 2\pi/\omega_0 \approx 155.3$ fs), although it is about three fourths of the oscillation period for the system considered here (see Fig. 2a). The discrepancy between these two characteristic vibrational periods is due to the anharmonicity of the Morse potential function. Notice that the wave packet energy expectation value $\langle\hat{H}\rangle$ is about $0.4D$. In such cases, the oscillation frequency between the two

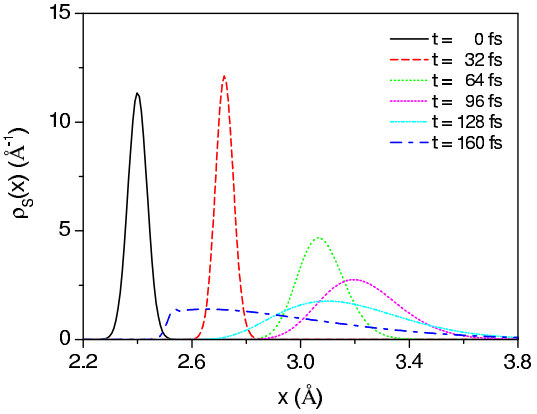

FIG. 1: Snapshots of the (averaged) reduced probability density within the first vibrational period (see Fig. 2a) inside the Morse potential (eq. 17) for negligible decoherence ($\Lambda = 10^{-8}$ a.u.). The initial state corresponds to the Gaussian wave packet (eq. 19). The times at which each snapshot was taken are indicated in the legend within the figure.

turning points of the Morse potential at a certain energy E is given by[34]

$$\omega_M = \omega_0 \sqrt{1 - \frac{E}{D}}. \tag{21}$$

Assuming that $E \sim \langle \hat{H} \rangle$, we obtain $\omega_M \sim 0.77\omega_0$, in agreement with the previous statement. The dynamics are therefore quite anharmonic, as seen in the figure: the wave packet spreading increases significantly along the propagation, contrary to the frozen oscillatory behavior displayed by the same wave packet in a harmonic potential.[35] This implies that, after some time, the foremost part of the wave packet will bounce backwards and overlap with the rearmost one, giving rise to the emergence of interference features (see the wave packet denoted with a blue dashed-dotted line).

The position expectation value $\langle \hat{x} \rangle(t)$ is represented in Fig. 2a and its oscillatory behavior provides us with a characteristic time scale for the system, namely $\bar{\tau} \approx$ 200 fs, which is in agreement with the value obtained through eq. 21, i.e., $\tau_M \sim 1.3\tau_0$. After substitution of the associated frequency $\bar{\omega} = 2\pi/\bar{\tau}$ into eq. 14, we find that the validity of the state vector approach is ensured in our case for $T \gg 60$ K. The curves displayed in this figure also provide us with an idea of how Λ influences the wave packet dynamics. As can be seen, for about two periods the position expectation value is not very sensitive to Λ; the damping observed in the oscillations is much more related to the anharmonicity of the potential than to decoherence. Decoherence effects become more relevant at around $t \approx 400{-}500$ fs, particularly for $\Lambda > 10^{-3}$. Notice that, in the long term, $\langle \hat{x} \rangle(t)$ does not approach the center of the well but displays a slight deviation to its right — towards the "softer" part of the Morse well. These values of Λ are of the order of 10^{28} cm^{-2}s^{-1} or higher, in agreement with the estimates provided by Joos and Zeh[36]

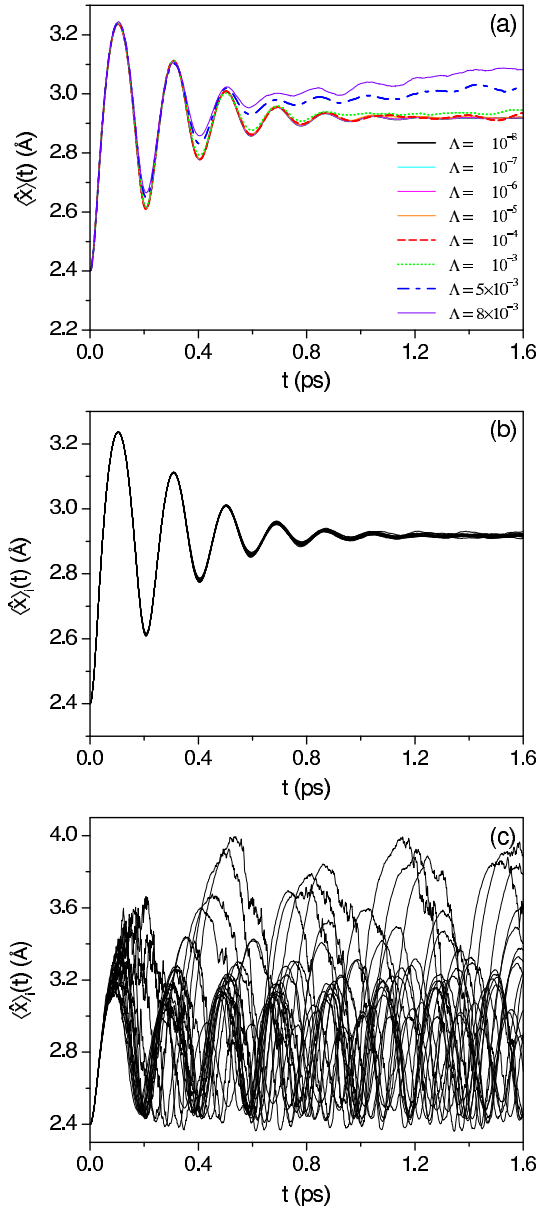

FIG. 2: (a) Position expectation value for different decoherence rates, from $\Lambda = 10^{-8}$ to 8×10^{-3} a.u. (b) Set of 20 quantum trajectories, $\langle \hat{x} \rangle_i(t)$, associated with the first 20 realizations of the Gaussian wave packet (eq. 19) for $\Lambda = 10^{-8}$ a.u. (c) The same as in Fig. 2b, but for $\Lambda = 5 \times 10^{-3}$ a.u.

for large molecules (with a size of $\sim 10^{-6}$ cm) acted on by air molecules at $T = 300$ K: $\Lambda \sim 10^{30}$ cm^{-2}s^{-1}.

The explanation for such a behavior can be readily understood by inspecting Figs. 2b and 2c for $\Lambda = 10^{-8}$ and $\Lambda = 5 \times 10^{-3}$, respectively. In each panel, a set of 20 quantum trajectories, $\langle \hat{x} \rangle_i(t)$, is displayed. For $\Lambda = 10^{-8}$, these trajectories essentially behave in the same way, not showing relevant deviations when one is compared with the others. In contrast, for $\Lambda = 5 \times 10^{-3}$, there are trajectories that display larger excursions towards the softer region of the potential well. It is this behavior

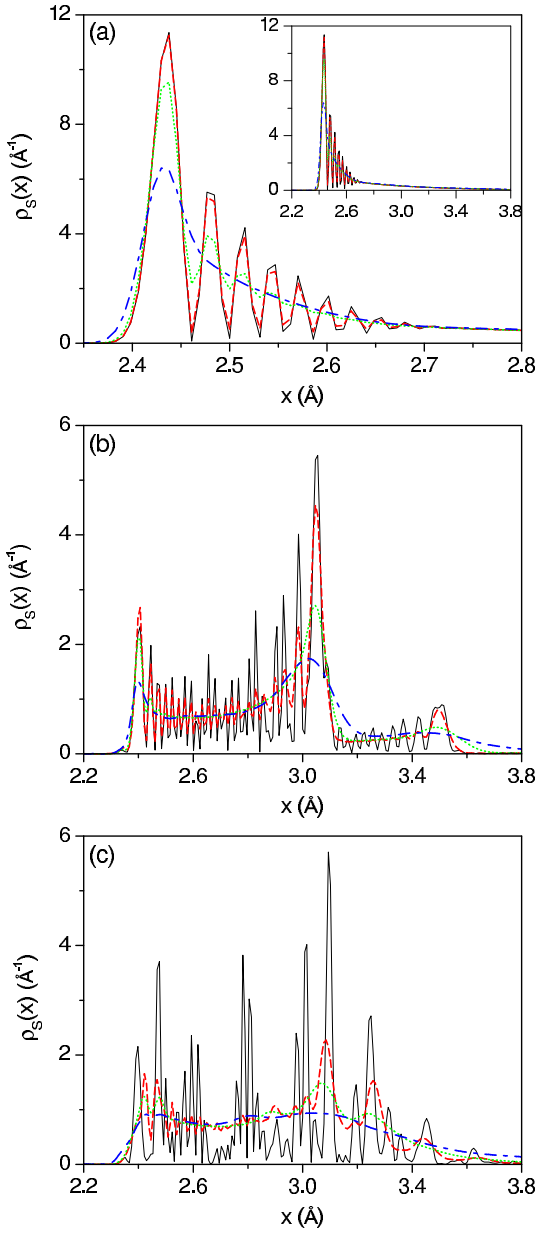

FIG. 3: Reduced probability density for different decoherence rates: $\Lambda = 10^{-8}$ a.u. (black solid line), $\Lambda = 10^{-4}$ a.u. (red dashed line), $\Lambda = 10^{-3}$ a.u. (green dotted line), and $\Lambda = 5 \times 10^{-3}$ a.u. (blue dashed-dotted line). (a) $t = 192$ fs, (b) $t = 640$ fs, and (c) $t = 1600$ fs. In Fig. 3a, the inset shows the long reach of the tail of the wave packet at $t = 192$ fs.

that eventually leads to the outwards displacement of the asymptotic value of $\langle \hat{x} \rangle$ observed in Fig. 2a.

To study now the decoherence effects induced by the bath on the system, three snapshots of the probability density have been represented in Fig. 3. The interference oscillations that can be seen in the three panels for $\Lambda = 10^{-8}$ constitute a signature of the system spatial quantum coherence, which is gradually lost as the system–bath coupling strength, Λ, increases. Thus, for $\Lambda = 10^{-3}$ and $\Lambda = 5 \times 10^{-3}$, a seemingly classical behavior is apparent: interference oscillations are totally suppressed and the distribution seems to be an "average" over the mean value of the totally coherent probability density. Indeed, it is this behavior that makes the right-hand-side "tail" of the distribution extend farther away for long times, provoking the deviation of $\langle \hat{x} \rangle(t)$ beyond 2.9 Å (see Fig. 2a).

Comparing Fig. 3 with figs. 4 and 5 from Wang et al.[4], we find that the state vector model is in good agreement with the forward-backward (FB) IVR results, which explicitly include the quantum dynamics of the bath degrees of freedom (described as Gaussian wave packets). In the simulations performed in Wang et al.[4], decoherence is analyzed essentially in terms of two bath-related parameters, namely friction (η) and temperature (T). Friction affects the system–bath coupling strength through the coupling coefficients c_j in the full Hamiltonian; temperature is varied by selecting the initial conditions according to a Boltzmann distribution at the corresponding temperature. In our case, as mentioned above, decoherence only depends on the rate Λ, since both η and T are included in it, as seen in (16). Nevertheless, even though we cannot make a separate analysis (which would allow us to determine the negligible effects of a finite coupling at $T = 0$, for example), a reliable comparison with the FB-IVR results is still possible by considering the quantity $\xi = \eta_e T$ (with $\eta_e \equiv \eta/m\omega_0$[4]).

Taking into account the above facts, we note that the state vector approach effectively captures and reproduces the physics of the more detailed FB-IVR analysis. For example, comparing Fig. 3a with fig. 4 from Wang et al.[4], we find that the calculation with $\Lambda = 10^{-3}$ a.u. produces an interference quenching similar to that observed for the cases with $\eta_e = 0.15$ and $T = 100$ K and $\eta_e = 0.05$ and $T = 300$ K for which $\xi = 15$. This result supports the fact that, at least in the case of thermal baths describable in terms of an ohmic spectral density, the crux of the matter regarding decoherence is the product ηT (or, equivalently, $\eta_e T$), as already pointed out by Elran and Brumer[37] by also using the FB-IVR method. That is, no matter which one of the two parameters is varied, the same decoherence effects will be essentially observed, provided their product ξ remains constant. This fact reinforces the use of the quantum state diffusion model, particularly eq. 15, where η and T appear combined together within the decoherence rate Λ. This property can be used to find out other analogous behaviors. For example, consider the cases for $\eta_e = 0.25$ with $T = 100$ and 300 K. For these, we find $\xi_{100} = 15$ and $\xi_{300} = 75$, respectively, with their ratio being $\xi_{300}/\xi_{100} = 5$. Given the proportionality between ξ and Λ, if $\xi = 15$ approximately corresponds to $\Lambda = 10^{-3}$, then $\xi = 75$ will correspond to a decoherence rate five times larger, i.e., $\Lambda = 5 \times 10^{-3}$. This is, effectively, what can be observed when the green dashed-dotted line in Fig. 3a is compared with the case with $\eta_e = 0.25$ and $T = 300$ K displayed in fig. 4 of Wang et al.[4]

For longer time scales (see Figs. 3b and 3c), we already

start noticing a smearing out of the probability density, which is not present in the FB-IVR results, although it is consistent with the typical exponential-like decay undergone by quantum coherence according to eq. 13[25]. Let us consider the following definition of coherence length:[36]

$$\ell(t) \equiv \left(\sqrt{8\Lambda t}\right)^{-1/2}, \tag{22}$$

which provides us with an estimate of the distance along which coherence is still preserved, and therefore information about the quenching of interference features. In Table I some estimates of the coherence length are given for $\Lambda = 10^{-4}$ and 10^{-3} at different times. In the case of $\Lambda = 10^{-4}$, as seen in the three panels of Fig. 3, the corresponding coherence lengths cover the width of at least several interference oscillations at their respective times. Hence interference features are still apparent even at $t = 1600$ fs. For $\Lambda = 10^{-3}$, however, only at $t = 192$ fs we can observe a series of weak interference oscillations, since the spatial coherence hardly covers the width of one oscillation. At later times, very weak interference features can be seen around $x \sim 2.4$ Å, where the width of the oscillations is still comparable with the coherence length.

Now, why is there a difference with respect to the FB-IVR simulations in spite of the consistency shown by the model? Here, one could be tempted to think whether the use of a limited set of harmonic oscillators in the FB-IVR is not producing a "fake" recoherence effect, since the Caldeira–Leggett model requires, in principle, an infinite collection of them. In other words, the description with a few oscillators may be valid for short times, but not for longer ones, as one may infer from the classical Wigner method.[38] For example, the largest frequency associated with these modes ($\omega_m = 100$ cm^{-1}) involves a characteristic time scale about twice as large as the Morse harmonic period. Therefore, after a number of such periods, it is reasonable to expect the appearance of recurrences, which may play a role by putting some coherence back into the system. Notice that the interaction between the system and each bath particle is relatively simple, and that there are no intrabath couplings, which at high temperatures give rise to faster decoherence rates.[39] This is easy to understand. As the bath temperature increases, not only is a faster transfer of coherence from the system to the bath expected but also that this coherence is more effectively transferred among different bath particles, something that cannot happen in the Caldeira–Leggett model because of its lack of intrabath couplings. In this sense, although a small number of bath oscillators (particles) seems to suffice for convergence in semiclassical simulations of the Caldeira–Leggett model,[4,37,40] avoiding possible classical recurrences, some coherence effects may still be active due to a lower transfer rate of this coherence among the bath degrees of freedom. Nevertheless, as acknowledged by Elran and Brumer,[37] it is also important to keep in mind that because of the hypothesis upon which Markovian models are built, they cannot cope with memory or backreaction. These effects may play an important role in the system dynamics, for example, at low temperatures or for a small number of bath particles (and relatively weak system–bath couplings). In this sense, there must always be a balance between one kind of approach and the others (full dynamical models and effective ones). They constitute different alternatives, but must also be complementary.

TABLE I: Coherence length (eq. 22) for different values of the decoherence rate and time.

Λ (a.u.)	t (fs)	ℓ (Å)
10^{-4}	192	0.21
	640	0.11
	1600	0.073
10^{-3}	192	0.066
	640	0.036
	1600	0.023

A plot of the reduced density matrix in configuration space, $\rho_S(x, x', t)$, also provides us with another interesting perspective on the decoherence process. In Fig. 4, the real and imaginary parts of this matrix (left and right columns, respectively, for each time) have been plotted at the same three times considered in Fig. 3 and for three decoherence regimes: negligible ($\Lambda = 10^{-8}$), moderate ($\Lambda = 10^{-3}$), and strong ($\Lambda = 5 \times 10^{-3}$). The real part of the reduced density matrix displays even symmetry with respect to the diagonal axis, $x = x'$, while its imaginary part is odd; the diagonal of the real part corresponds to the probability density (see Fig. 3a), while the diagonal of the imaginary one vanishes. In both cases, the most remarkable feature is the chessboard-like structure due to interference. As Λ increases, this structure fades out and a stripe-like structure emerges. These stripes, parallel to the axis $x = x'$, denote the persistence of some amount of quantumness. As the value of Λ increases even more, this structure also disappears, only surviving the terms close to the diagonal (even though some small off-diagonal contributions can still persist in the imaginary part of the reduced density matrix).

B. Two-state superposition dynamics

The analysis of the system dynamics studied in the previous section in terms of populations and coherences is also very interesting, since it takes us from the configuration space to an energy representation. When the Gaussian wave packet of the previous section is recast as a superposition of eigenfunctions of the Morse oscillator,[41,42] about 70 of the approximately 120 bound states supported by this potential contribute to the wave packet dynamics. Analyzing the behavior of the associated populations and coherences will then be more confusing than clarifying. Hence, instead, we are going to consider a se-

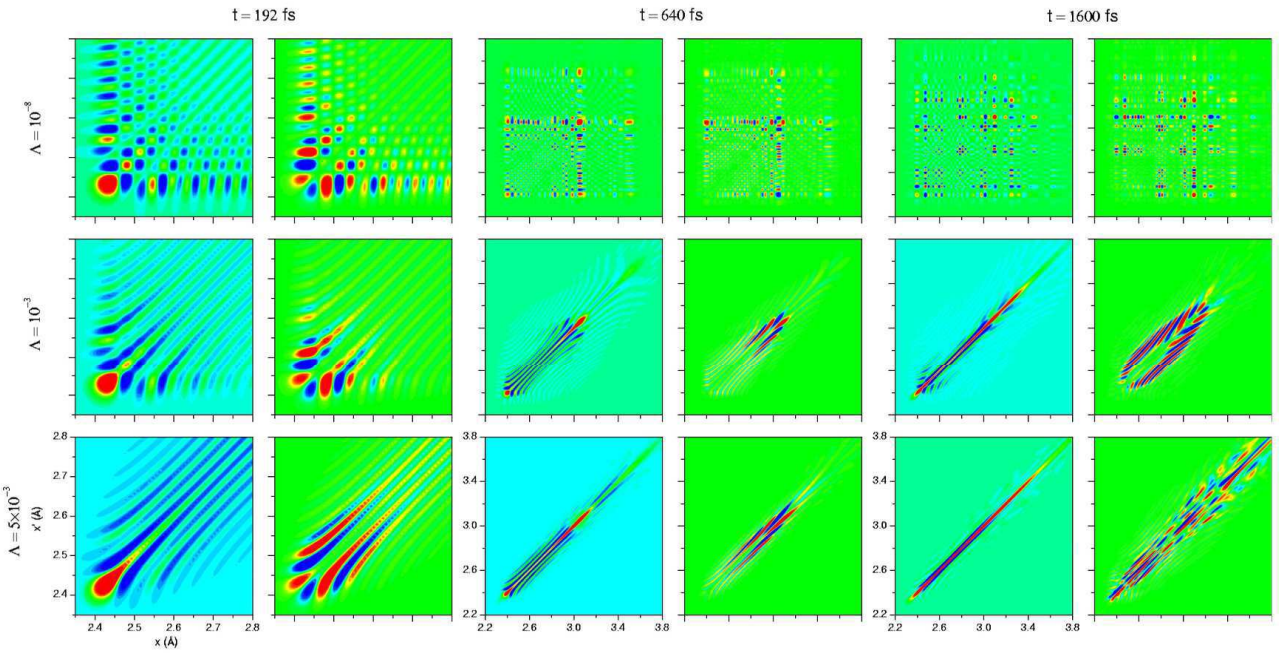

FIG. 4: Density matrix in configuration space at t = 192, 640, and 1600 fs. At each time, left/right panels represent the real/imaginary part of the density matrix. Different decoherence rates: $\Lambda = 10^{-8}$, 10^{-3}, and 5×10^{-3}. The color scale, from blue to red, indicates the transition from minimum (negative) to maximum (positive) values.

ries of different two-state superpositions, in particular with low-energy states, for which a total of 2000 realizations is enough to obtain converged results. As the initial wave function, we will use

$$\Psi_{mn,0}(x) = c_m \Phi_m(x) + c_n \Phi_n(x), \tag{23}$$

where m and n label the corresponding Morse eigenfunctions. In all cases, we have considered (i) $n > m$, (ii) $c_m^2 = 0.4$ and $c_n^2 = 0.6$ to have a biased superposition, and (iii) a moderate decoherence regime, with $\Lambda = 9 \times 10^{-3}$ Å^{-2}fs^{-1} ($\sim 6.1 \times 10^{-5}$ a.u.), which produces a substantial quenching of the interference features along the propagation, but without fully suppressing them ($\ell \approx 0.068$ Å).

The first quantity of interest that we are going to analyze is the purity:

$$\begin{aligned} \chi(t) &= \mathrm{Tr}[\hat{\rho}_{\mathrm{S}}^2(t)] = \sum_{i,j} \langle \Phi_i | \hat{\rho}_{\mathrm{S}}(t) | \Phi_j \rangle \langle \Phi_j | \hat{\rho}_{\mathrm{S}}(t) | \Phi_i \rangle \\ &= \sum_i |\langle \Phi_i | \hat{\rho}_{\mathrm{S}}(t) | \Phi_i \rangle|^2 + \sum_{i \neq j} |\langle \Phi_j | \hat{\rho}_{\mathrm{S}}(t) | \Phi_i \rangle|^2, \end{aligned} \tag{24}$$

which is a measure of the degree of "mixedness" of the system quantum state[3] or, within our context, of the incoherence among different realizations. Notice that this dephasing as well as the fact that other states apart from Φ_n and Φ_m may become populated with time will lead to $\chi(t) \leq 1$ as time increases (at $t = 0$ and/or $\Lambda = 0$, $\chi = c_n^2 + c_m^2 = 1$). To understand the sensitivity of the decoherent process to Λ and more specifically the choice of the initial state, in Fig. 5a, we have plotted the time evolution of χ for a (0,3)-superposition and the Gaussian wave packet considered in Section IV A for two values of Λ. As can be seen, for a given value of Λ, the larger amount of eigenstates involved in the dynamics of the Gaussian wave packet produces a decay of its purity faster than for Ψ_{03}. Actually, while χ decays smoothly for the superposition, a series of steps or oscillations are noticeable in the case of the Gaussian state. This decay, as is seen for higher Λ, takes place in two time scales rather than one, as confirmed by a best-fit analysis with one and two decaying exponential functions. In the first case, decay times of about 111 fs for Ψ_{03} and 103 fs for the Gaussian have been obtained, with fitting correlation factors of 0.928 and 0.979, respectively. In the second case, decay times of about 61 and 998 fs for Ψ_{03}, and 94 and 804 fs for the Gaussian have been obtained, with correlations of 0.999 and 0.982, respectively (obviously, the substantially better agreement for Ψ_{03} was expected due to the lack of oscillations in its χ-function). Again, these facts can also be determined from FB-IVR calculations, as shown by Elran and Brumer[37] (see fig. 4 in this work, when the fluctuating behavior of the graphs is neglected and one focuses only on their average trend).

In order to investigate now the bath effects on the system depending on the components of the initial superposition, in Fig. 5b, we have plotted $\chi(t)$ for Ψ_{03}, Ψ_{05}, and Ψ_{36} (for comparison, the graph for the Gaussian state has also been included). As can be seen, the decay of the purity becomes faster as the components forming the

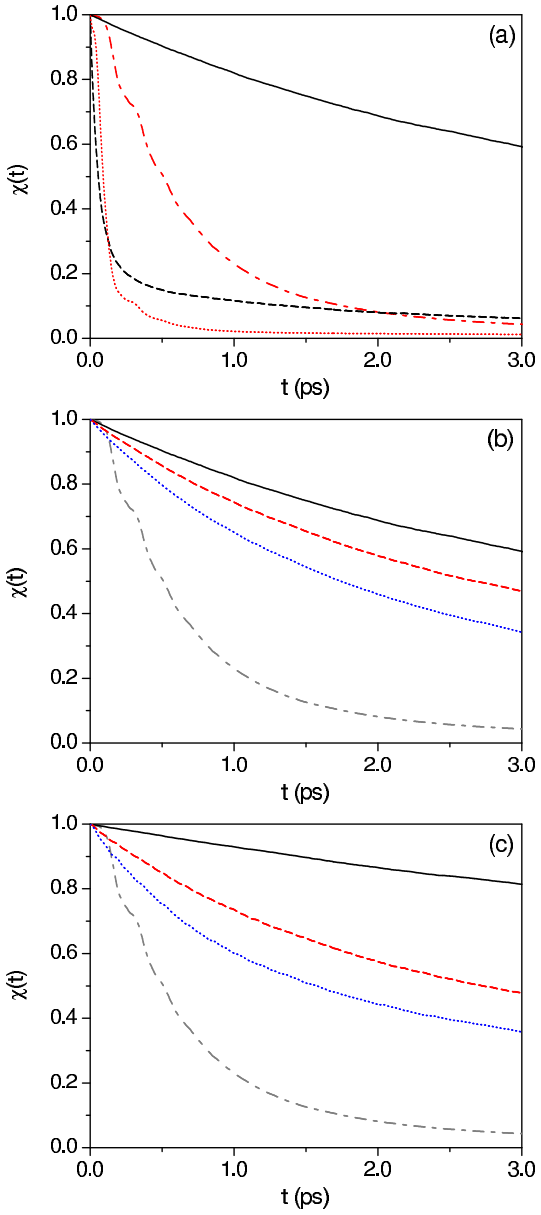

FIG. 5: (a) Time evolution of χ for Ψ_{03} and $\Lambda = 9 \times 10^{-3}$ Å^{-2}fs^{-1} (black solid line), Ψ_{03} and $\Lambda \approx 0.74$ Å^{-2}fs^{-1} (black dashed line), a Gaussian and $\Lambda = 9 \times 10^{-3}$ Å^{-2}fs^{-1} (red dash-dotted line), and a Gaussian and $\Lambda \approx 0.74$ Å^{-2}fs^{-1} (red dotted line). (b) Time evolution of χ for Ψ_{03} (black solid line), Ψ_{05} (red dashed line), and Ψ_{36} (blue dotted line). (c) Time evolution of χ for Ψ_{01} (black solid line), Ψ_{45} (red dashed line), and Ψ_{89} (blue dotted line). In Figs. 5b and 5c, $\Lambda = 9 \times 10^{-3}$ Å^{-2}fs^{-1} and, to compare with, the time evolution of χ for a Gaussian wave packet (gray dashed-dotted line) under the same conditions has also been included.

superposition are higher in energy. This explains why the purity for the Gaussian state decays so quickly with respect to the superpositions: initially, considering only those states whose populations are ≥ 0.01, we have a superposition of 34 eigenstates, from Φ_{12} to Φ_{46}. Now, given that these eigenstates are consecutive in energy, one may ask about the decay for two-state superpositions of this kind. Results for the superposition states Ψ_{01}, Ψ_{45}, and Ψ_{89} are displayed in Fig. 5c and, as expected, as the energy increases, the decay of χ becomes faster. However, this decay is not homogeneous, although the energy levels are consecutive in all superpositions. As can be noticed, the distance between χ_{01} and χ_{45} is larger than between χ_{45} and χ_{89}. This could be connected to the fact that the relative difference, defined as

$$\Delta_{mn} = \left(\frac{En - E_m}{E_n} \right) \times 100\%, \tag{25}$$

is larger in the case of the (0,1)-superposition ($\sim 66\%$) than for the other two ($\sim 22\%$ for Φ_{45} and $\sim 11\%$ for Φ_{89}). A smaller difference between energy levels means a larger recurrence time $\tau_{mn} = 2\pi\hbar/(E_n - E_m)$ and, therefore, a higher susceptibility to be acted by decoherence, which is precisely what we observe in the figure (notice that $\tau_{01} \approx 157$ fs, $\tau_{45} \approx 162$ fs, and $\tau_{89} \approx 167$ fs). From a best-fit to a single decaying exponential, we find that the decay times are $\bar{\tau}_{01} \sim 6.4$ ps for Φ_{01}, $\bar{\tau}_{45} \sim 2.0$ ps for Φ_{45}, and $\bar{\tau}_{89} \sim 1.2$ ps for Φ_{89}. The ratios of these characteristic times, $\bar{\tau}_{01}/\bar{\tau}_{45} \sim 3.2$ and $\bar{\tau}_{45}/\bar{\tau}_{89} \sim 1.7$, actually seem to be consistent with the ratios between relative differences, $\Delta_{01}/\Delta_{45} \sim 3$ and $\Delta_{45}/\Delta_{89} \sim 2$.

According to eq. 24, χ may decay because of a change in the populations:

$$P_i(t) = \rho_{S,ii}(t) = \langle \Phi_i | \hat{\rho}_S(t) | \Phi_i \rangle, \tag{26}$$

or the suppression of the coherences:

$$\zeta_{ij}(t) = |\rho_{S,ij}(t)|^2 = |\langle \Phi_i | \hat{\rho}_S(t) | \Phi_j \rangle|^2, \tag{27}$$

or both effects at the same time.[43] In order to determine which one of these possibilities occurs, consider Fig. 6, where the population dynamics associated with the superposition states Ψ_{03} (Fig. 6a) and Ψ_{36} (Fig. 6b) are displayed. For simplicity, only the levels with populations equal to or larger than 0.01 at $t = 3$ ps are displayed. We find that higher-energy levels decay faster (the decay of the ground-level population in Fig. 6a is negligible), in agreement with the fact that purity decays faster for higher-energy superpositions. Now, at the same time that these levels decay, others become gradually populated. Here, both examples confirm that the level occupation follows the rule $m+1$, $m-1$, $n+1$, $n-1$, $m+2$, ... Indeed, if two-state superpositions formed by consecutive energy levels are considered, as seen in Fig. 7, a similar rule is found, although the level that becomes populated in the second place corresponds to the lower-energetic state of the superposition. This is the reason why we observe an increase of P_0 with time in Fig. 7b. Nonetheless, the occupational rule of new states in this case is $m+1$, $n-1$, $m+2$, ...

To complete the picture, in Fig. 8 the coherence dynamics for the elements ρ_{03} of the (0,3)-superposition and ρ_{36} for the (3,6)-superposition are displayed. From the

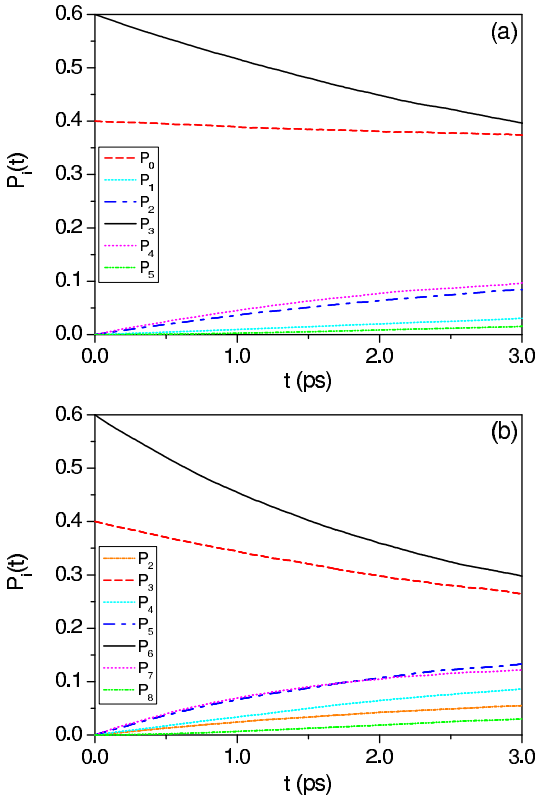

FIG. 6: Population dynamics for (a) Ψ_{03} and (b) Ψ_{36}. In both graphs, the population for the higher-energy state of the superposition is denoted by the black solid line and the lower-energy state with the red dashed line; other incipient states have been denoted with different types of line/color (see the legend in each case). Only the populations such that $P_i(t) \geq 0.01$ at $t = 3$ ps have been plotted.

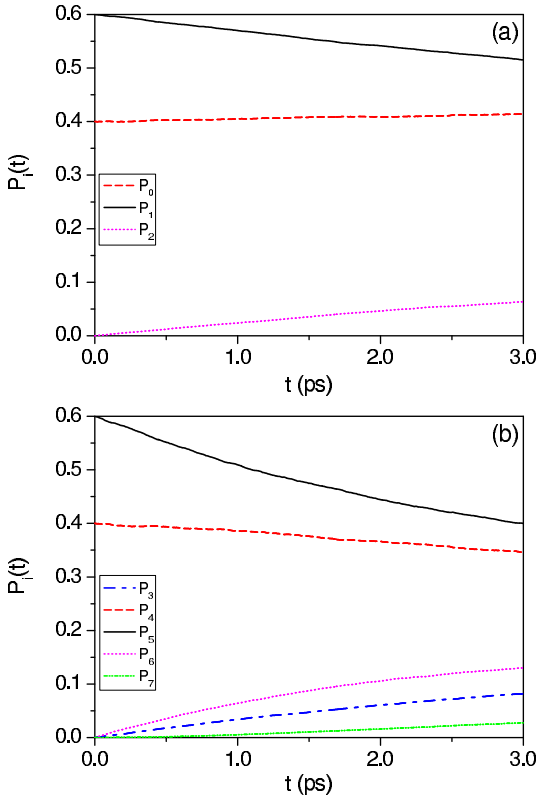

FIG. 7: Population dynamics for (a) Ψ_{01} and (b) Ψ_{45}. In both graphs, the population for the higher-energy state of the superposition is denoted by the black solid line and the lower-energy state with the red dashed line; other incipient states have been denoted with different types of line/color (see the legend in each case). Only the populations such that $P_i(t) \geq 0.01$ at $t = 3$ ps have been plotted.

calculations, it was observed that only these elements are the most strongly influenced, with their damping being again correlated with the energy of the levels involved. Although some other off-diagonal elements start developing, they are still very small (smaller than 10^{-4}) at $t = 3$ ps and therefore negligible regarding effects related to coherence dynamics.

Taking these facts into account, we can conclude that the decay of purity comes essentially from a population redistribution (diagonal terms of the density matrix in the energy representation), including other states that were not present in the initial superposition, and a decay of the coherence (off-diagonal terms of the density matrix) between the two initial states of the superposition. As has been observed, at least in the cases analyzed (and for the propagation time considered), although new levels start becoming populated, no coherence appears among them. Since the coherence between the two initial states is also gradually lost, $\hat{\rho}_S$ becomes asymptotically a diagonal matrix, in agreement with the findings of the previous section (see the long-time calculations displayed in Fig. 4 for large decoherence rates). In other words, in the long time regime, the second term (in the second line) of eq. 24 is expected to vanish, so that this expression becomes

$$\chi_\infty \approx \sum_i |\langle \Phi_i | \hat{\rho}_{S,\infty} | \Phi_i \rangle|^2 = \sum_i P_{i,\infty}^2, \qquad (28)$$

which is always smaller than 1 (unless only one state becomes populated in the end). Actually, it is also expected that population dynamics reach an equilibrium, eventually distributing in a Boltzmann fashion. To get a glimpse of this guess, some calculations for Ψ_{03} with $\Lambda \approx 0.74$ Å^{-2}fs^{-1} (5×10^{-3} a.u.) have been run in order to more quickly reach the asymptotic regime. These calculations seem to support the fact that populations approach an equilibrium value, with the energy levels being occupied in inverse relation to their energy (see Fig. 9), although at short times, the occupancy rule mentioned above is again confirmed (see inset).

V. FINAL REMARKS

In this work, the quantum state diffusion approach has been used to analyze the decoherence dynamics in the vibrational motion of I_2. In spite of the limitations of

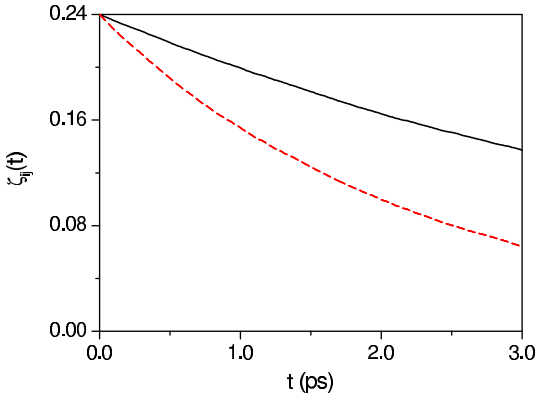

FIG. 8: Coherence dynamics, ζ_{ij}, for Ψ_{03} (black solid line) and Ψ_{36} (red dashed line). Other incipient coherences have not been represented because they are negligible ($\leq 10^{-5}$).

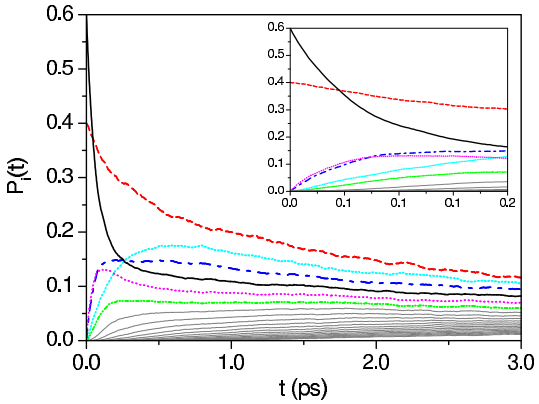

FIG. 9: Population dynamics for Ψ_{03} and $\Lambda \approx 0.74$ Å^{-2}fs^{-1}. The level populations for Φ_3 and Φ_0 are denoted by the black solid line and red dashed line, respectively. Other line colors/types are as in Fig. 6a; gray lines denote populations for levels $5 \leq i \leq 19$, for which $P_i \geq 0.01$. Inset: detail of the short-time dynamics.

this model, we have seen that it constitutes an interesting tool to explore in a simplified manner the decoherence dynamics of systems affected by thermal baths, without abandoning any of the important elements involved in larger and more detailed calculations (e.g., FB-IVR). Indeed, the results obtained are in good agreement with those reported in the literature from such types of calculations.[4,37]

Regarding the computational cost involved in the type of calculations considered here, it is worth stressing that, compared with a standard, wave packet unitary propagation, the multiple-realization process involved in solving eq. 15 (for the same propagation time) is essentially equivalent to performing consecutively N of such unitary propagations (the stochastic part is relatively low time-consuming, since it does not involve additional nonlocal evaluations associated with functions of the momentum operator $\hat{p}$, as happens with the Hamiltonian $\hat{H}$). This feature, together with the fact that each realization is independent, makes the scheme suitable for parallelization, thus increasing its time efficiency. Compared with other methods, it is worth noticing that the FB-IVR calculations used in Wang et al.[4] required a total of 5×10^4 to 10^5 $2(M+1)$-dimensional realizations in order to reach convergence. Each one of these realizations involves the two classical degrees of freedom of the system (x, p) and those of the oscillators (Q_i, P_i), with $i = 1, 2 \ldots, M$ (about 20-40 oscillators were needed by the authors to properly describe the continuous spectral density assumed in Wang et al.[4]). Putting aside the time consumed in evaluating the monodromy matrix elements required by the FB-IVR, the computation of such a number of $2(M+1)$-dimensional classical trajectories is relatively demanding,[37] even though the oscillators are not coupled among themselves, as happens in more realistic bath models.[38,39] In this regard, solving eq. 15 is advantageous both computationally and interpretively, since it is less time-consuming and provides a similar degree of accuracy (when properly tuned), as seen in Section IV A.

There are a few issues that are left open in this work but on which there is currently some preliminary work in progress. First, the application of this methodology to other contexts of interest, for example, scattering systems, such as slit systems[9,44] and atom-surface collisions,[45,46] where it is shown that the standard textbook guess of only varying some typical quantum parameter to reach the classical limit is not valid.[47] Second, and more importantly, how to link in a systematic fashion this approach to more exact calculations and to more realistic systems.[38,39] In this work, the value of the decoherence rate Λ has been changed because we had the freedom to choose the coefficient $\xi = \eta T$ and compare it with results available in the literature. However, it is highly desirable to find out a way to determine this quantity in a unique manner once the nature of the bath is specified (e.g., type of system–bath and bath–bath interactions) and its physical conditions are defined (e.g., temperature). Notice that depending on the bath nature, the influence over the system will be different[39] even for the same (bath) physical conditions. In this sense, the form of the Lindblad operators should also be analyzed, since the position operator may be valid for bilinear couplings (as is the case of the Caldeira–Leggett model), but not in more complex situations (e.g., interactions of diatomics with rare gas liquids or solid matrices).

Acknowledgments

This work is dedicated to Paul Brumer, a good man and an excellent teacher, with all my affection and admiration. The author thanks the Chemical Physics Theory Group of the University of Toronto for kind access to its computational facilities, as well as the Ministerio de Economía y Competitividad (Spain) for economical support under Project FIS2011-29596-C02-01 and a "Ramón y Cajal" Research Grant.

[1] Breuer, H.-P.; Petruccione, F. *The Theory of Open Quantum Systems* Oxford: Oxford University Press, 2002.

[2] Giulini, D.; Joos, E.; Kiefer, C.; Kupsch, J.; Stamatescu, I.-O.; Zeh, H. D., Eds. *Decoherence and the Appearance of a Classical World in Quantum Theory*. Berlin: Springer, 1996; 2nd ed.

[3] Schlosshauer, M. *Decoherence and the Quantum-to-Classical Transition*. Berlin: Springer, 2007.

[4] Wang, H.; Thoss, M.; Sorge, K. L.; Gelabert, R.; Giménez, X.; Miller, W. H. *J. Chem. Phys.* **2001**, 114, 2562.

[5] Miller, W. H. *J. Chem. Phys.* **1970**, 53, 3578.

[6] Miller, W. H. *Faraday Discuss.* **1998**, 110, 1.

[7] Miller, W. H. *J. Phys. Chem. A* **2001**, 105, 2942.

[8] Miller, W. H. *J. Chem. Phys.* **2012**, 136, 210901.

[9] Gelabert, R.; Giménez, X.; Thoss, M.; Wang, H.; Miller. W. H. *J. Chem. Phys.* **2001**, 114, 2572.

[10] Diósi, L. *J. Phys. A* **1988**, 21, 2885.

[11] Diósi, L. *Phys. Lett. A* **1988**, 129, 419.

[12] Wiseman H. M.; Diósi, L. *Chem. Phys.* **2001**, 268, 91.

[13] Gisin, N.; Percival, I. C. *J. Phys. A* **1992**, 25, 5677.

[14] Gisin, N.; Percival, I. C. *J. Phys. A* **1993**, 26, 2245.

[15] Gisin, N.; Knight, P. L.; Percival, I. C.; Thompson, R. C.; Wilson, D. C. *J. Mod. Opt.* **1993**, 40, 1663.

[16] Percival, I. C. *Quantum State Diffusion*. Cambridge: Cambridge University Press, 1998.

[17] Carmichael, H. *An Open Systems Approach to Quantum Optics*. Berlin: Springer, 1993.

[18] Sanz, A. S.; Miret-Artés, S. *A Trajectory Description of Quantum Processes. I. Fundamentals*. Berlin: Springer, 2012.

[19] Sanz, A. S.; Miret-Artés, S. *A Trajectory Description of Quantum Processes. II. Applications*. Berlin: Springer, 2013.

[20] Itô, K. *Foundations of Stochastic Differential Equations in Infinite Dimensional Spaces*. Philadelphia, PA: SIAM, 1984.

[21] Ikeda, N.; Watanabe, S. *Stochastic Differential Equations and Diffusion Processes*. Amsterdam: North-Holland, 1989, 2nd ed.

[22] To be more precise in this regard, rather than using the term "classical", it should be said in analogy to the solutions of ordinary differential equations (of which the equations of classical mechanics are just a particular type). Partial differential equations, like Schrödinger's equation or eq. 5, describe the propagation of field-type variables and therefore the concept of trajectory is ambiguous unless some criterion is properly defined. For example, within quantum state diffusion, trajectories are defined as the expectation value of some operator. This means that, given a particular initial wave function, there is always a multiplicity of trajectories, as many as realizations are considered. If $\hat{\mathcal{O}} = \hat{x}$, each trajectory corresponds to the position expectation value obtained from each independent, stochastic realization of the state vector $|\Psi\rangle_i$, which here is denoted by $\langle\hat{x}\rangle_i(t)$ (see Section IV A). As another example, in Bohmian mechanics[18,19] for the same initial wave function one has that for a single realization there are as many trajectories as chosen initial conditions; these initial conditions are taken in such a way that the positions are distributed according to the corresponding probability density and the momenta are fixed by the initial phase of the wave function. In this case, trajectories would be labeled as $x_i(t)$ (like "classical" trajectories), with the position expectation value being the average over a large ensemble of these trajectories, i.e., $\langle\hat{x}\rangle(t) = (1/N)\sum_{i=1}^{N} x_i(t)$.

[23] Accardi, L.; Lu, Y. G.; Volovich, I. *Quantum Theory and its Stochastic Limit*. Berlin: Springer, 2002.

[24] Zurek, W. H.; Habib, S.; Paz, J. P. *Phys. Rev. Lett.* **1993**, 70, 1187.

[25] Joos, E. In *Decoherence and the Appearance of a Classical World in Quantum Theory*; Giulini, D.; Joos, E.; Kiefer, C.; Kupsch, J.; Stamatescu, I.-O.; Zeh, H. D., Eds. Berlin: Springer, 1996, 2nd ed.; p. 41180.

[26] Gong, J.; Brumer, P. *Phys. Rev. E* **1999**, 60, 1643.

[27] Prezhdo, O. V. *Phys. Rev. Lett.* **2000**, 85, 4413.

[28] Han, H.; Brumer, P. *J. Chem. Phys.* **2005**, 122, 144316.

[29] Feit, M. D.; Fleck, J. J. A.; Steiger, A. *J. Comput. Phys.* **1982**, 47, 412.

[30] Feit, M. D.; Fleck, J. J. A. *J. Chem. Phys.* **1983**, 78, 301.

[31] Feit, M. D.; Fleck, J. J. A. *J. Chem. Phys.* **1984**, 80, 2578.

[32] Press, W. H.; Teukolsky, S. A.; Vetterling, W. T.; Flannery, B. P. *Numerical Recipes: The Art of Scientific Computing*. New York: Cambridge University Press, 2007, 3rd ed.

[33] Klauder, J. R.; Petersen, W. P. *SIAM J. Numer. Anal.* **1985**, 22, 1153.

[34] DeMarcus, W. C. *Am. J. Phys.* **1978** 46, 733.

[35] Sanz, A. S.; Miret-Artés, S. *Chem. Phys. Lett.* **2007**, 445, 350.

[36] Joos, E.; Zeh, H. D. *Z. Phys. B* **1985**, 59, 223.

[37] Elran, Y.; Brumer, P. *J. Chem. Phys.* **2004**, 121, 2673.

[38] Elran, Y.; Brumer, P. *J. Chem. Phys.* **2013**, 138, 234308.

[39] Sanz, A. S.; Elran, Y.; Brumer, P. *Phys. Rev. E* **2012**, 85, 036218.

[40] Goletz, C.-M.; Grossmann, F. *J. Chem. Phys.* **2009**, 130, 244107.

[41] Morse, P. M. *Phys. Rev.* **1929**, 34, 57.

[42] Mündel, C.; Domcke, W. *Chem. Phys.* **1989**, 105, 137.

[43] Sanz, A. S.; Han, H.; Brumer, P. *J. Chem. Phys.* **2006**, 124, 214106.

[44] Hornberger, K.; Uttenthaler, S.; Brezger, B.; Hackermüller, L.; Arndt, M.; Zeilinger, A. *Phys. Rev. Lett.* **2003**, 90, 160401.

[45] Pollak, E.; Miret-Artés, S. *J. Chem. Phys.* **2009**, 130, 194710.

[46] Moix, J. M.; Pollak, E.; Miret-Artés, S. *Phys. Rev. Lett.* **2010**, 104, 116103.

[47] Sanz, A. S.; Borondo, F.; Miret-Artés, S. *Europhys. Lett.* **2001**, 55, 303.